CORA Cork Open Research Archive
Cartlann Taighde Oscailte Chorcaí

Title	Monolithic InGaAs nanowire array lasers on silicon-on-insulator operating at room temperature
Authors	Kim, Hyunseok;Lee, Wook-Jae;Farrell, Alan C.;Morales, Juan S. D.;Senanayake, Pradeep;Prikhodko, Sergey V.;Ochalski, Tomasz J.;Huffaker, Diana L.
Publication date	2017-05-23
Original Citation	Kim, H., Lee, W. J., Farrell, A. C., Morales, J. S., Senanayake, P., Prikhodko, S. V., Ochalski, T. J. and Huffaker, D. L. (2017) 'Monolithic InGaAs nanowire array lasers on silicon-on-insulator operating at room temperature', Nano Letters, 17(6), pp. 3465-3470. doi: 10.1021/acs.nanolett.7b00384
Type of publication	Article (peer-reviewed)
Link to publisher's version	10.1021/acs.nanolett.7b00384
Rights	© 2017, American Chemical Society. This document is the Accepted Manuscript version of a Published Work that appeared in final form in Nano Letters, 17(6), pp. 3465-3470, after technical editing by the publisher. To access the final edited and published work see: https://doi.org/10.1021/acs.nanolett.7b00384
Download date	2026-11-15 17:12:27
Item downloaded from	https://hdl.handle.net/10468/14967

UCC
University College Cork, Ireland
Coláiste na hOllscoile Corcaigh

Supporting Information

Monolithic InGaAs nanowire array lasers on silicon-on-insulator operating at room temperature

Hyunseok Kim[1], Wook-Jae Lee[2], Alan C. Farrell[1], Juan S. D. Morales[3,4], Pradeep Senanayake[1], Sergey V. Prikhodko[5], Tomasz J. Ochalski[3,4] and Diana L. Huffaker[1,6,7]*

[1]Department of Electrical Engineering, University of California Los Angeles, Los Angeles, California 90095, United States

[2]School of Engineering, Cardiff University, Cardiff CF24 3AA, United Kingdom

[3]Centre for Advanced Photonics and Process Analysis, Cork Institute of Technology, Cork T12 P928, Ireland

[4]Tyndall National Institute, University College Cork, Cork T12 R5CP, Ireland

[5]Department of Material Science and Engineering, University of California Los Angeles, Los Angeles, California 90095, United States

[6]California Nano-Systems Institute, University of California Los Angeles, Los Angeles, California 90095, United States

[7]School of Physics and Astronomy, Cardiff University, Cardiff CF24 3AA, United Kingdom

I. Design of nanowire array cavity on planar SOI layer

II. Rate equation analysis

III. Design of nanowire array cavity on SOI mesas

IV. Growth of InGaAs/InGaP core/shell nanowires

V. Characterization of InGaAs/InGaP core/shell nanowires

VI. Coupled mode analysis of nanowire array laser

VII. References

I. Design of nanowire array cavity on planar SOI layer

In this section, the design of nanowire cavities on planar SOI substrates is demonstrated in detail. The schematic illustration of the nanowire cavity is shown in Fig. S1a. The nanowire array forms a 1D nanobeam cavity, which employs a photonic bandgap (PBG) in one dimension (*x*-axis) and total internal reflection (TIR) in the other dimensions (*y*- and *z*-axis) to achieve optical confinement. It is already well demonstrated that the artificial defect of the nanobeam cavities can be formed in various ways, such as the modulation of air-hole diameters, wrist widths, and periods[1-3]. Here we choose to form the artificial defect by modulating the period of the nanowires while keeping the dimension of all nanowires constituting the cavity equal. The period of nanowires in the taper section is modulated gradually to minimize the radiation loss[1], and the offset of the graded taper is fixed to 10 nm ($p = p_1+50 = p_2+40 = p_3+30 = p_4+20 = p_5+10$) due to the resolution of the e-beam writing setup we used. The effect of the number of total nanowires N on the cavity Q is shown in Fig. S1b. 3D FDTD simulations (FDTD Solutions, Lumerical) are conducted to calculate Q factors. The cavity Q is 970 without reflector nanowire array ($N = 11$), which increases as the number of nanowires constituting the reflector increases. Because the cavity Q saturates around 80,000 for $N \geq 21$, we have chosen $N = 21$ for our design. The SOI layer thickness (t) of 40 nm, the nanowire diameter (a) of 140 nm, the nanowire height (h) of 800 nm, and the period (p) of 350 nm is used for the simulations, which are close to the dimension of the fabricated laser in the manuscript.

The out-of-plane confinement along the *y*- and *z*-axis is another requisite to achieve high cavity Q. Although the nanowire/air interface along the *y*-axis satisfies the TIR condition due to high index contrasts, the confinement along the *z*-axis is degraded by the underlying silicon, because the refractive index of silicon is larger than the effective refractive index of the nanobeam cavity and the TIR condition is not satisfied. We propose two approaches in the manuscript to achieve vertical confinement, (1) by using a thin SOI layer which is further analyzed in this section, and (2) by using a patterned SOI layer which is further analyzed in Supporting Section III. As a first approach, integrating nanowire cavities on thin SOI layers can

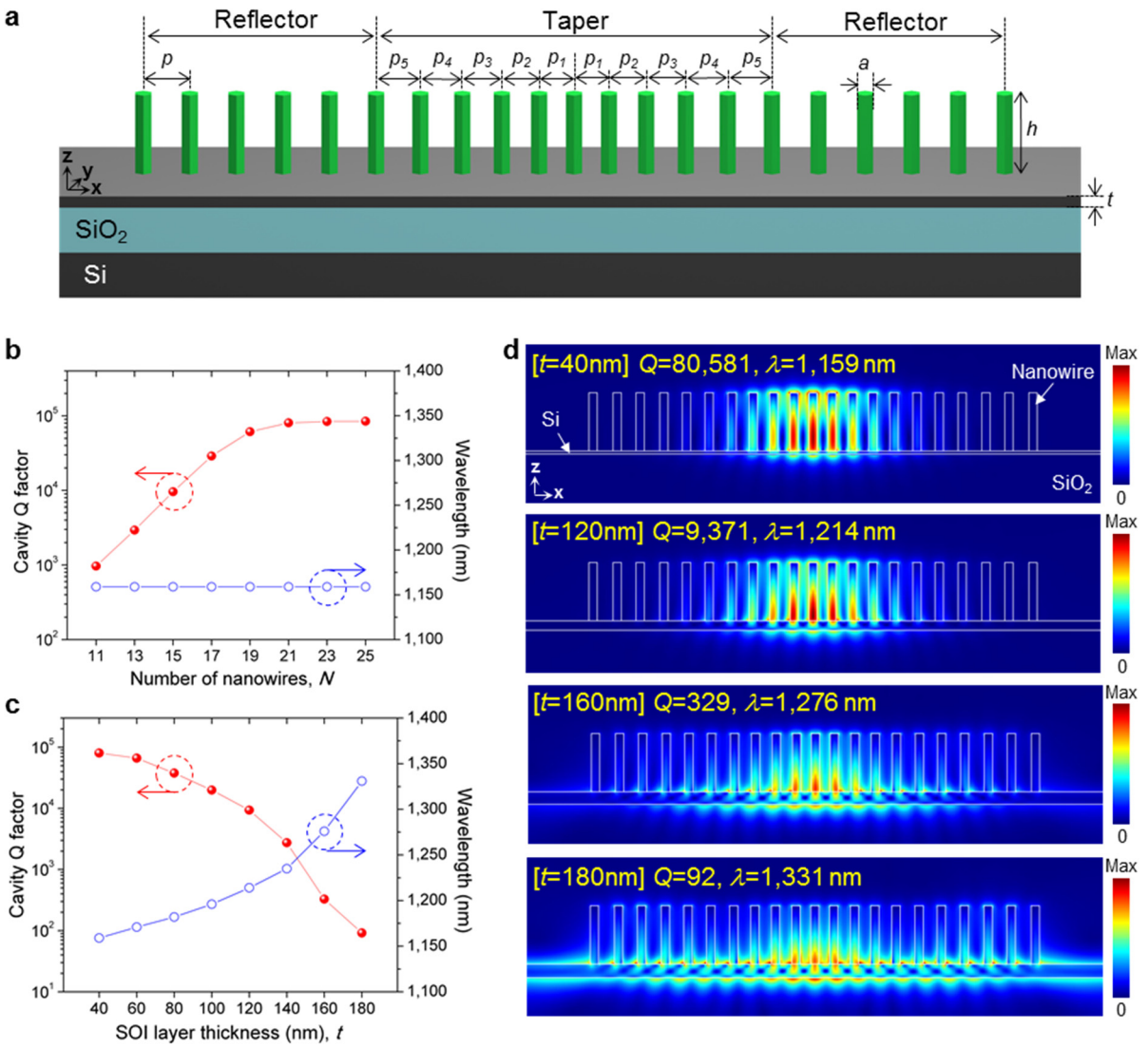


Figure S1. Design of nanowire array cavity on planar SOI layer. a, Schematic of the nanowire array cavity. **b**, Dependence of the number of total nanowires (N) on the cavity Q. **c,d**, Dependence of the SOI layer thickness (t) on the cavity Q, and electric field intensity profiles showing worse confinement at larger t.

circumvent this problem by minimizing the leakage through silicon. The effect of the SOI layer thickness (t) on the cavity Q is shown in Fig. S1c. The cavity Q rapidly decreases by increasing t, and the cavity Q becomes less than 1,000 when t > 140 nm. A confined mode is not observed anymore at t > 180 nm. As shown in the electric field profile in Fig. S1d, the overlap of the field with silicon increases and the resonant wavelength becomes longer as t gets thicker. It is also clearly shown in the electric field profile at t = 160 nm and t = 180 nm that the field is leaking out of the cavity through the SOI layer. In our design, a thin SOI

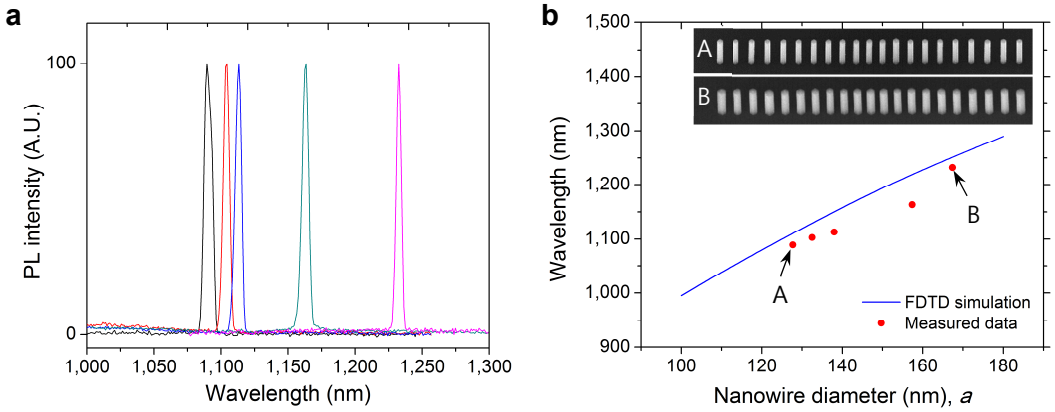


Figure S2. Diameter-dependence of lasing wavelengths. a, PL spectra of five nanobeam arrays with p = 350 nm. **b**, Comparison of measured lasing wavelengths with FDTD simulations.

layer of t = 40 nm is employed for the nanowire cavity.

One of the advantages of our approach is that the lasing wavelength can be controlled lithographically. If the nanowire diameter (d) is increased or decreased, the lasing wavelength also increases or decreases due to the change of the effective refractive index of the nanobeam cavity. Modifying the period (p) also shifts the lasing wavelength, as the period determines the lattice constant of the 1D photonic crystal. Here, the effect of nanowire diameters on lasing wavelengths is experimentally demonstrated. Five lasing spectra shown in Fig. S2a are measured from five different nanobeam lasers with the same period (p = 350 nm) but different diameters. As shown in Fig. S2b, lasing wavelengths from these lasers match reasonably well with theoretical cavity mode wavelengths calculated by 3D FDTD simulations. These results verify that the lasing wavelength can be tuned by lithographically varying the diameter of nanohole patterns, which determines the diameter of as-grown nanowires. It is worth mentioning that the nanobeam laser emitting at 1,230 nm is achieved by growing InGaAs nanowires with higher indium composition (33 %) to shift the gain spectrum to longer wavelengths. Based on these results, we believe that telecom-wavelength (1.3 − 1.55 μm) lasing will also be possible by adjusting the cavity geometry, growing InGaAs nanowires with higher indium composition, and growing shells which are lattice-matched to InGaAs core with increased indium content.

II. Rate equation analysis

In order to estimate the spontaneous emission factor (β) and Q factor of the nanowire array laser on a thin SOI layer, we used modified rate equations based on refs 4 and 5 to investigate the lasing behavior under optical pumping conditions. Carrier density (N) in the active nanowires (11 nanowires in the tapered area) and photon density (S) in the cavity mode are described as follows:

$$\frac{dN}{dt} = \frac{\eta P}{\hbar\omega_p V} - AN - \frac{N}{\tau_{sp}} - CN^3 - v_g GS \quad (1)$$

$$\frac{dS}{dt} = \left[\Gamma v_g G - \frac{1}{\tau_p}\right] S + \Gamma\beta\frac{N}{\tau_{sp}} \quad (2)$$

where the material gain (G) is given by a logarithmic model, $G(N) = g_0 \ln\frac{(N+N_s)}{(N_{tr}+N_s)}$. P and V are the optical pump power and volume of the active nanowires, respectively. N_{tr}, N_s, and g_0 are obtained by fitting the peak gain calculated by modelling (LaserMOD, Rsoft) based on the measured photoluminescence (PL) spectrum as shown in Fig. S3. All parameters used are listed in Table S1. We assume η = 0.01, which is the fraction of the pump light absorbed by the active nanowires, considering our optical characterization setup. Fig. S4a shows the plot of L-L curves calculated from the rate equations.

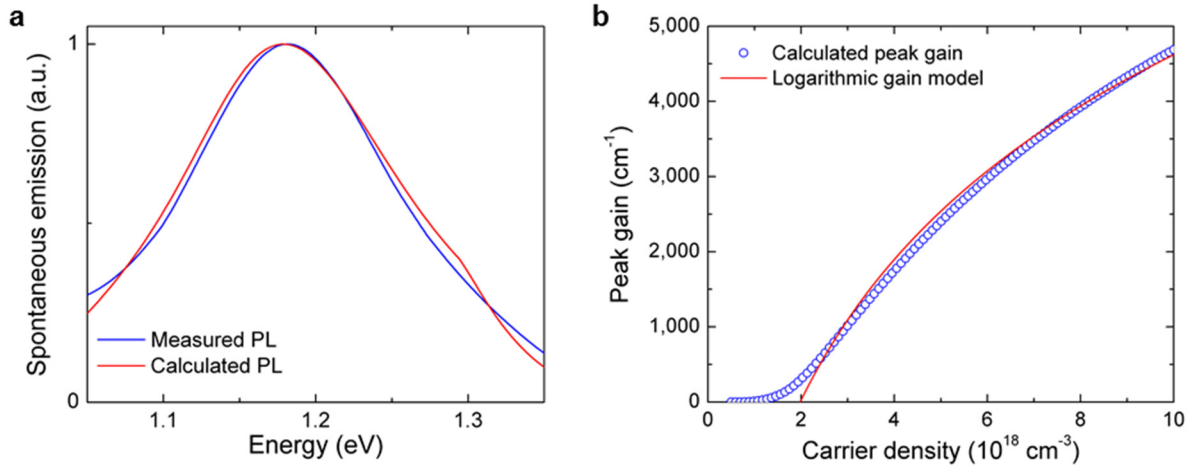


Figure S3. Fitting spontaneous emission for gain modelling. a, The PL spectrum of nanowires and the calculated spectrum ($In_{0.2}GaAs$ with the relaxation energy of 0.15 eV) showing the fit. **b**, Calculated peak gain and logarithmic material gain model as a function of carrier density.

Table S1: Parameters used in the rate equations	
Fraction of the pump light absorbed by the active nanowires (η)	0.01
Nonradiative recombination coefficient (A)	1.43×10^{8} s^{-1}
Auger recombination (C)	3.5×10^{-30} $cm^{6}s^{-1}$
Spontaneous emission lifetime (τ_{sp})	4 ns
Group index (n_g)	4
Gain coefficient (g_0)	3250 cm^{-1}
Transparency current density (N_{tr})	1.98×10^{18}
Third linearity parameter (N_s)	5.71×10^{17}
Confinement factor (Γ)	0.637
Frequency of pump laser ($\omega_p=2\pi c/\lambda$)	2.854×10^{15}

It should be noted that the Q factor is also a fitting parameter in this analysis, because calculating the Q factor from the cavity linewidth is difficult due to (1) the abrupt change of the linewidth around the transparency carrier density[5] and (2) the broadening of the linewidth under pulsed operation[6]. The best fitting values for β and Q factor are 0.0065 and 1,150, respectively. These β and Q factors are derived by pumping the center of the nanobeam photonic crystal cavity, with a pump spot size of 1.8 μm. This indicates that the pump area overlaps with approximately seven nanowires in the center. As shown in the electric field profile in Fig. 1b in the manuscript, almost the entire field of the lasing mode is confined in these seven nanowires in the center. Therefore, the confinement factor Γ will be almost identical with the case of pumping the entire nanowires. On the other hand, the cavity Q factor will be affected by the pump area, because nanowires outside the pumping area are absorptive at the lasing wavelength which is beyond their bandgap energy. If nanowires in reflector sections are pumped together with nanowires in the center, the material loss of reflector sections will decrease by pumping, which will lead to an increase of the cavity Q

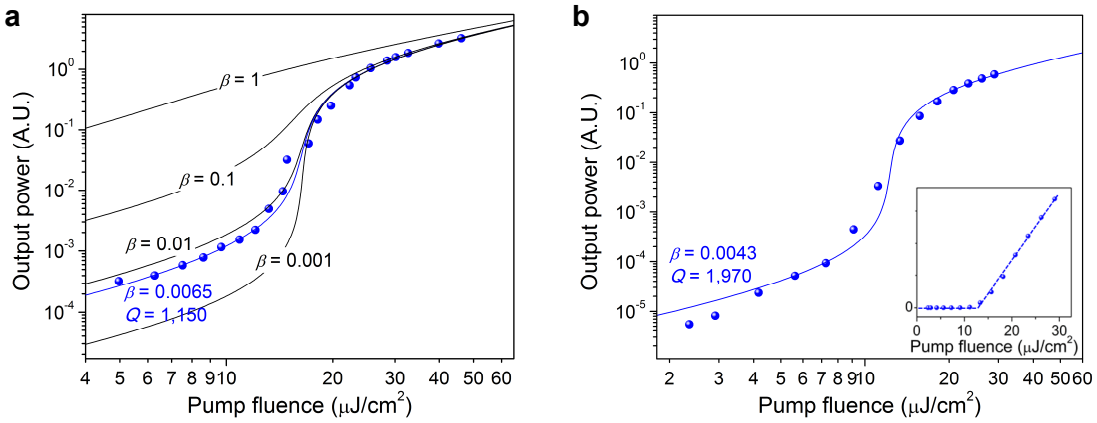


Figure S4. Rate equation analysis. a, Rate equation modellings for various spontaneous emission factors β. The L-L curve calculated with β = 0.0065 and Q = 1,150 fits the best with experimental data. **b**, Double-logarithmic L-L curve measured by homogeneously pumping entire nanowires. β = 0.0043 and Q = 1,970 fits the best with experimental data. Inset: Experimental L-L curve shown in a linear scale.

factor and a decrease of lasing threshold. This speculation is verified by measuring the L-L curve by pumping the entire nanowire arrays. A cylindrical lens (f = 50 cm) is inserted into the pump beam path to form an elliptical pump beam shape on the sample. The beam spot size is measured to be 10.5 μm (major axis, x-direction) and 1.8 μm (minor axis, y-direction), which covers the entire array (6.7 × 0.14 μm^2).

Fig. S4b shows the L-L curve measured by pumping the same nanowire array shown in Fig. 1 and 2 in the manuscript and in Fig. S4a, with a cylindrical lens but keeping other conditions identical. Rate equation fitting reveals that the Q factor is increased from 1,150 to 1,970, while β is decreased from 0.0065 to 0.0043. The threshold pump fluence is decreased from 16 μJ/cm^2 to 12 μJ/cm^2 by pumping the entire array (inset in Fig. S4b), as the Q factor is increased. We attribute the decrease of β to a reduction of the portion of emitted photons coupled into the lasing mode, as the spontaneous emission from nanowires in reflector sections does not contribute to lasing.

The Q factors derived from rate equation fittings are 1,150 and 1,970 for different pumping conditions, which are more than an order of magnitude smaller than the Q factor derived from FDTD simulations. This is primarily stemming from the fabrication imperfections in nanowire cavities. When non-uniformity in the

nanowire dimension is considered in simulations (standard deviation of 5 nm in nanowire diameters and 20 nm in nanowire heights), the Q factor is calculated to be 1,045, which is similar with the measured Q factors. This suggests that a more robust cavity design or improved growth conditions are required to realize high-Q bottom-up nanowire array cavities.

III. Design of nanowire array cavity on SOI mesas

SOI wafers with a silicon thickness of 220 nm have become the standard for silicon photonic foundries around the world[7]. The capability to integrate light sources on 220 nm-thick SOI substrates is thus crucial to ensure compatibility with silicon photonic platforms. As demonstrated in Supporting Section I, however, the SOI layer needs to be quite thin ($t \leq 140$ nm) in order to achieve strong vertical confinement for lasing operation in the proposed nanowire cavity design. We propose a new architecture to achieve high-Q nanowire cavities on 220 nm-thick SOI substrates, which is realized by integrating nanowires on SOI mesas. As shown in the schematic illustration in Fig. S5a, each nanowire is positioned on the center of rectangular mesas, where each mesa with a width of w is pre-patterned by e-beam lithography and dry etched before nanowire epitaxy. This architecture is analogous to the design in Supporting Section I if we regard the mesa as a part of the nanobeam cavity providing the in-plane optical feedback. We can infer from the simulations in Supporting Section I that the cavity Q will be enhanced by decreasing the thickness of the etched SOI layer (t). Given that the SOI layer thickness is fixed to 220 nm for the compatibility with silicon photonics platforms, increasing the depth of the etched trench d (which is the height of mesas) leads to the decrease of t. This speculation is verified with FDTD simulations in Fig. S5b. Confined modes are observed when $t \geq 60$ nm, and the cavity Q increases by making the trench deeper. The parameters $a = 140$ nm, $h = 800$ nm, $p = 300$ nm, and $w = 150$ nm are chosen for the simulation. As shown in the electric field profiles in Fig. S5c, the field leaks through the silicon when d is small (t is large), which is very similar with the case of the nanowire array cavity on thick SOI planes (Fig. S1d). Similarly, the overlap of the field with silicon

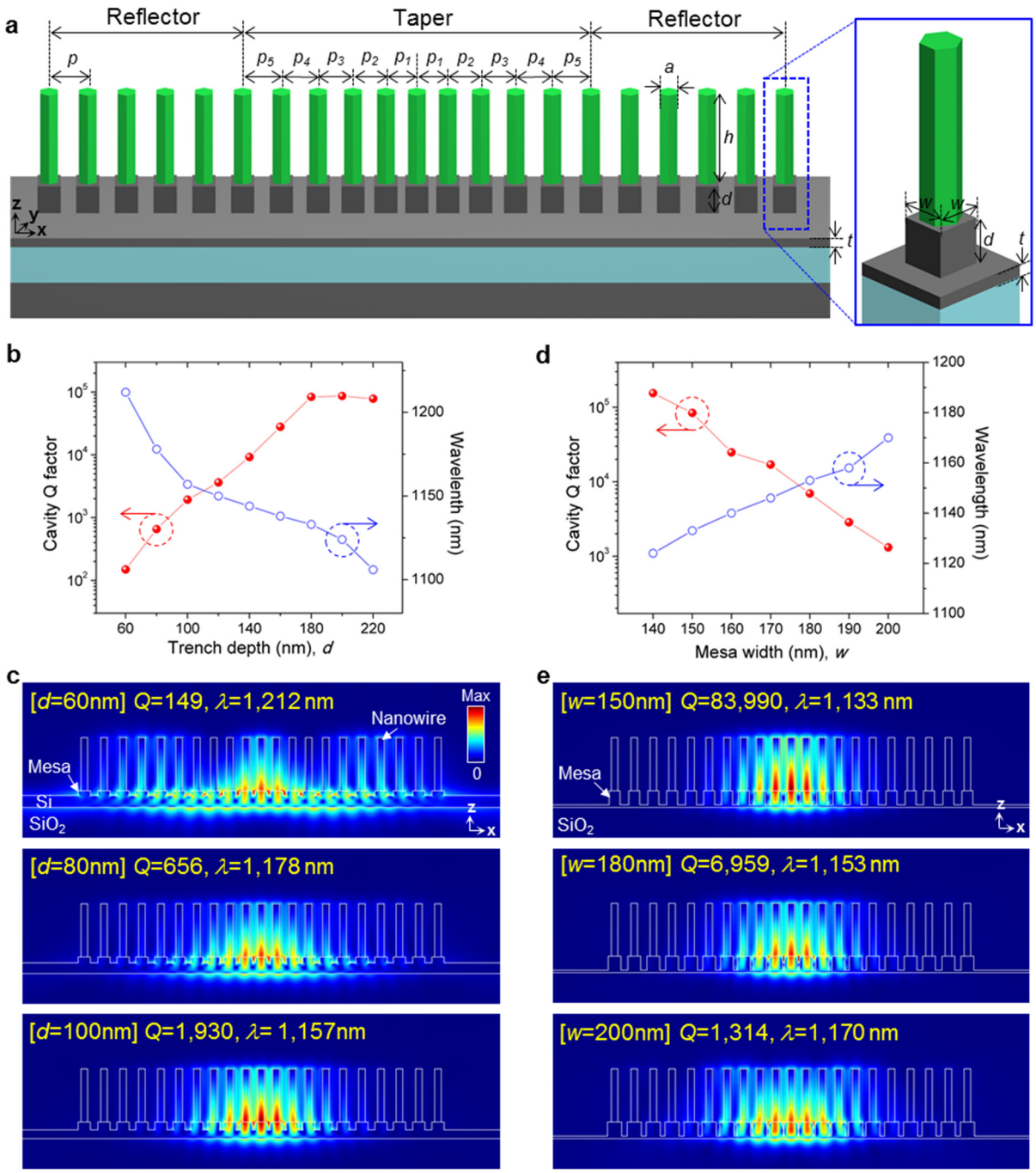


Figure S5. Design of nanowire array cavity on SOI mesas. a, Schematic of the nanowire array cavity. **b,c**, Dependence of the trench depth (d) on the cavity Q, and electric field intensity profiles showing worse confinement at smaller d. **d,e**, Dependence of the mesa width (w) on the cavity Q, and related electric field intensity profiles.

increases by enlarging the size of mesas, which degrades the cavity Q (Fig. S5d and Fig. S5e). We adopt w = 150 nm for our devices, because the width of mesas needs to be larger than the diameter of nanowires for

epitaxy. The mesa height of d = 180 nm (t = 40 nm) is employed, so that the mesas can be patterned simultaneously with SOI rib waveguides without any additional process. The proposed nanowire cavity on SOI mesas exhibits a cavity Q ~ 83,000 and confinement factor Γ ~ 0.51 at the peak wavelength of 1,133 nm.

It should also be noted that changing the mesa width (w) shifts the cavity peak wavelength, as shown in Fig. S5d, in addition to the nanowire diameter (a) and pitch (p) which is already discussed in Supporting Section I. This provides an additional degree of freedom and flexibility in controlling the lasing wavelengths, and suggests the possibility of the proposed platform for wavelength division multiplexing (WDM).

For the nanowire array lasers to be truly compatible with silicon photonic platforms and PICs and suitable for practical applications, the lasers have to be integrated on SOI(001) substrates instead of SOI(111). Although the growth of nanowires on SOI(001) was not demonstrated in this work, there has been studies on growing vertical nanowires on Si[8] or III-V wafers[9-11] with (001) orientations, by employing growth templates or controlling growth conditions. These results suggest that the proposed bottom-up nanobeam design is not necessarily limited to (111)-oriented substrates, and can potentially be integrated onto SOI(001) platforms.

IV. Growth of InGaAs/InGaP core/shell nanowires

InGaAs/InGaP core/shell nanowires are grown on both patterned SOI and flat SOI substrates by metal-organic chemical vapor deposition (MOCVD). A lightly p-doped (Boron, 10 Ω.cm) 6-inch SOI (111) wafer (SEH America Inc., USA) with an SOI layer thickness of 450 nm and a buried oxide layer thickness of 2 μm is used for the nanowire growth. The SOI thinning, etching, and nanohole patterning processes are the same as our previous report[12]. 20 nm-thick silicon nitride (Si_3N_4) is used as a dielectric mask for selective-area epitaxy, and the diameter of exposed nanoholes was ~ 70 nm. The SEM image in Fig. S6a shows the nanoholes patterned on SOI mesas. The sample was cleaned by 6:1 buffered oxide etch solution for 30 secs

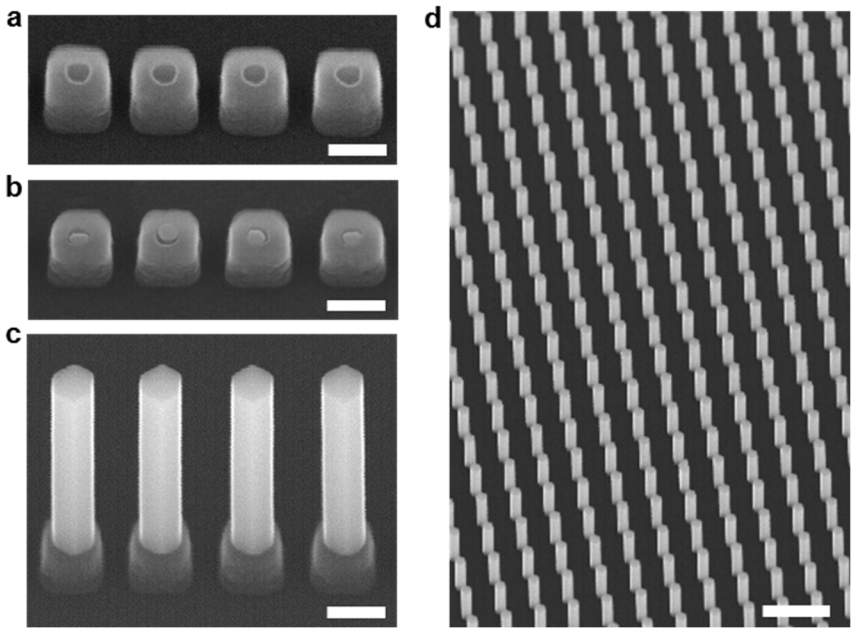


Figure S6. Nanowire growth on SOI. a-c, Nanowire growth on SOI mesas by nanoholes patterning on SOI mesas (**a**), GaAs stub growth in nanoholes (**b**), followed by InGaAs nanowire growth (**c**). Scale bars, 500 nm. **d**, Nanowire array grown on planar SOI. Scale bar, 1 μm. All SEM images are measured by tilting the sample 30˚ from the normal direction.

to remove the native oxide right before growth.

A low-pressure (60 Torr) vertical reactor (Emcore D-75) is used for the MOCVD growth. Triethylgallium (TEGa), trimethylindium (TMIn), tertiarybutylarsine (TBAs), and tertiarybutylphosphine (TBP) are used as precursors and hydrogen is used as a carrier gas. The reactor temperature is first ramped up to 880 °C and held for 13 mins under hydrogen ambient for thermal de-oxidation. A short GaAs stub is grown at 680 °C for 3 mins, followed by the InGaAs core growth at 680 °C for 11 mins. The nanowires are passivated *in-situ* by growing InGaP shells for 45 secs at 600 °C. The gas phase indium composition (In/(In+Ga)) was 0.29 for the InGaAs core growth and 0.75 for the InGaP shell growth. The molar flow rates and V/III flow rate ratios of each segment are mentioned in the Methods section of the manuscript.

We have introduced small GaAs stubs before the growth of InGaAs nanowires, because growing InGaAs nanowires directly on Si surfaces was not successful in achieving good vertical growth yield. On the other hand, InGaAs nanowires grown on top of the small GaAs stubs (Fig. S6b) resulted in high vertical

growth yield (> 99 %), as shown in the large InGaAs nanowire array in Fig. S6d.

V. Characterization of InGaAs/InGaP core/shell nanowires

The nanowires integrated on SOI mesas are sliced by focused ion beam (FIB) etching for cross-sectional energy dispersive x-ray spectroscopy (EDX) as depicted in the scanning transmission electron microscopy (STEM) image in Fig. S7a. Platinum is used as a glue for the sample preparation. Line-scan measurements along the axial and radial direction are conducted to characterize the material content and compositional uniformity of core/shell nanowires. The spatial resolution of EDX measurement is estimated to be 18 nm, and accelerating voltage of 300 kV is used.

The line-scan data along the radial direction in Fig. S7b show that only In counts increases while Ga and As counts decrease around the edge of the nanowire. Corresponding In and As compositions in Fig.

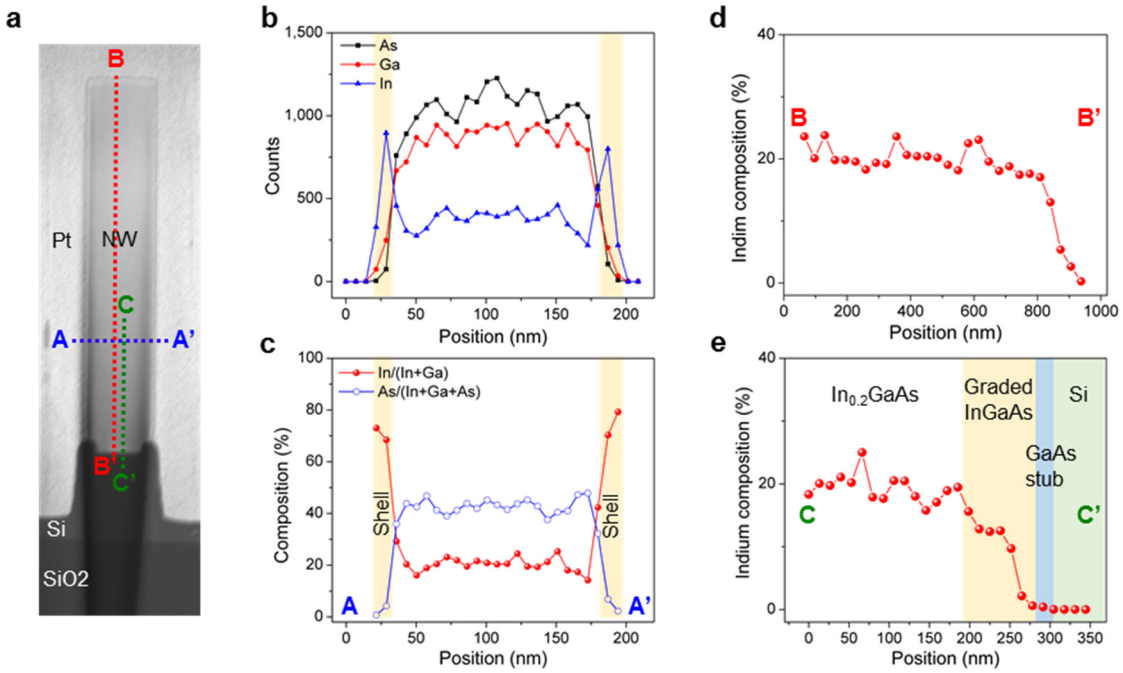


Figure S7. EDX analysis of InGaAs/InGaP core/shell nanowires on SOI. a, Low-resolution STEM image of the nanowire cross-section. **b,c**, Photon counts along the radial direction (A-A') (**b**), and In and As compositions calculated from the photon counts (**c**). **c,d**, In/(In+Ga) composition along the axial direction (B-B') (**d**) and (C-C') (**e**)

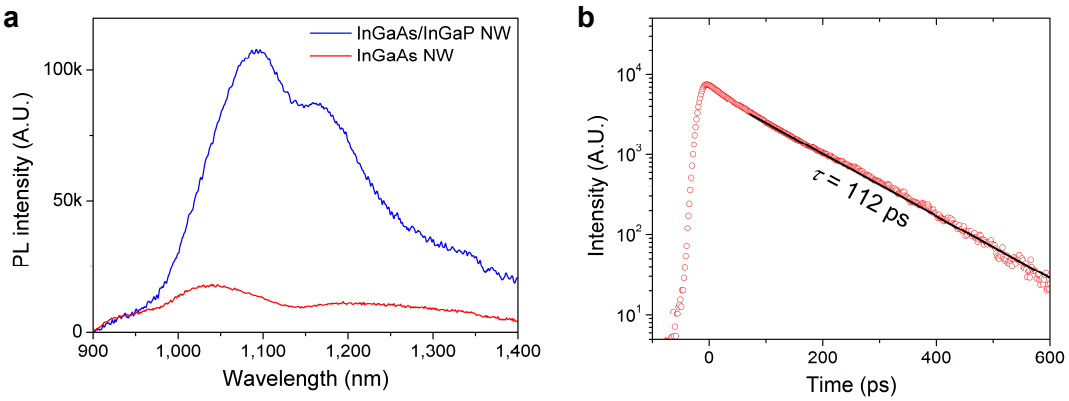


Figure S8. Effect of InGaP shell passivation. a, PL spectra of InGaAs nanowires with and without InGaP surface passivation measured at room temperature. **b**, Time-resolved photoluminescence measurement of InGaAs/InGaP core/shell nanowires.

S7c show that an InGaP shell with approximately 75 % In composition is grown around the InGaAs core with approximately 20 % In composition. Transition of the group V material from arsenic to phosphorous in the shell is deduced from As composition because the energy of x-ray photons from phosphorous overlaps with the energy from platinum, which makes the P counts unreliable. The $In_{0.75}GaP$ shell is closely lattice-matched with the $In_{0.2}GaAs$ core (mismatch ~ 0.5 %). The axial line-scan data across the entire nanowire (Fig. S7d) also confirms that the indium composition of InGaAs core is around 20 % except around the interface with the substrate. A close-up line-scan measurement around the interface is conducted to further investigate the composition of the nanowires, as shown in Fig. S7e. A gradual increase of indium composition above the GaAs stub is observed around the bottom 80 nm part of the nanowire, which is attributed to the In segregation during the growth[13]. The fluctuation and segregation of indium portion in nanowires will lead to a broadening of gain spectra, and this will increase the threshold pump power.

The effect of *in-situ* passivated InGaP shells is also confirmed from μPL and time-resolved PL (TRPL) measurements. First, the μPL from InGaAs/InGaP core/shell nanowires are compared with InGaAs nanowires without the shell. The InGaAs nanowire sample is grown under the same growth condition, only excluding the shell growth step. Both samples are pumped by a continuous 632 nm He-Ne laser with a pump power of 30 μW. A 50× objective lens is used to pump nanowires and collect the emission, and a

large array (50 × 50 μm) of nanowires with 500 nm pitch is measured to exclude the influence of beam alignment to the PL intensity. As shown in Fig. S8a, the PL intensity from InGaAs/InGaP core/shell nanowires is around sixfold larger compared with nanowires without passivation.

TRPL measurements are conducted at room temperature by pumping nanowires using a Ti-Sapphire laser with a wavelength of 790 nm, pulse duration of 300 fs, and repetition rate of 75.6 MHz as an excitation source. The emission from nanowires are measured using a streak camera (Hamamatsu C5680) with a resolution of 3 ps. The room-temperature minority carrier lifetime of InGaAs/InGaP core/shell nanowires is estimated to be 112 ps (Fig. S8b), while that of InGaAs nanowires without shell is measured to be 20 ps (data not shown). Although emission intensities and minority carrier lifetimes are significantly increased (both by a factor of more than five) by surface passivation, the measured lifetime is still as low as 112 ps. We have recently shown that InGaAs nanowires grown on GaAs substrates can exhibit room-temperature lifetime of up to 1 ns by *in-situ* surface passivation[14], which implies that the quality of surface passivation can be further improved by optimizing growth conditions.

Internal quantum efficiency (IQE), which is defined as the ratio of radiative recombination to total recombination, is extracted from rate equations-based analyses[15,16]. This method does not require any assumption about the absorption efficiency of nanowires, absolute pump density, or *A*, *B* and *C* coefficients in rate equations. Pump intensities and corresponding total spontaneous emission intensities (both in arbitrary units) are the only required parameters for the IQE fitting. First, pump intensities and emission intensities are fitted using the following equation,

$$P_{in} = P_1\sqrt{I_{SE}} + P_2 I_{SE} + P_3 I_{SE}^{\frac{3}{2}} \quad (3)$$

, where P_{in} is the pump power, I_{SE} is the total spontaneous emission intensity, and P_1, P_2 and P_3 are fitting parameters. Then, IQE can be directly calculated as

$$IQE = \frac{P_2 I_{SE}}{P_{in}}. \quad (4)$$

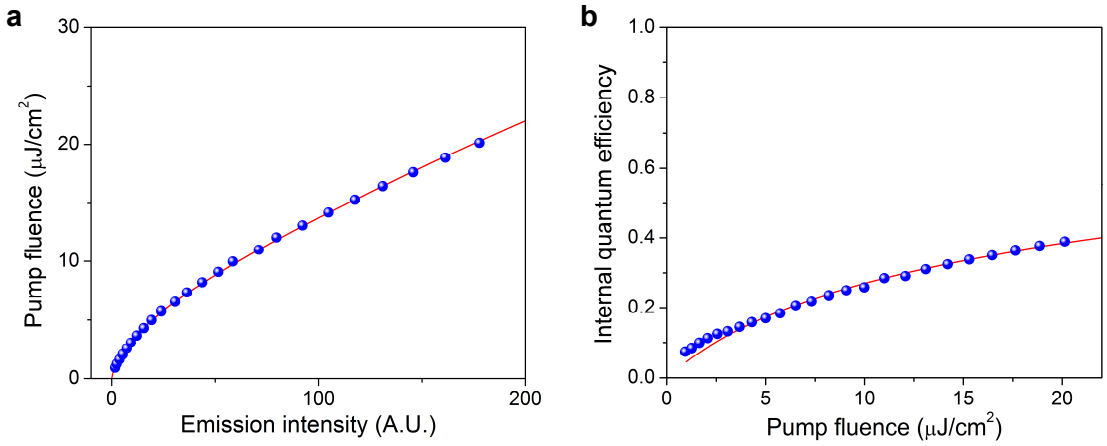


Figure S9. Internal quantum efficiency (IQE) of nanowires. a, Spontaneous emission intensity of nanowires plotted with pump fluence (blue circle), and rate equation fitting (red line). **b**, IQE as a function of pump fluence calculated from measurement data (blue circle) and fitting parameters (red line).

To extract IQE, P_{in} and I_{SE} are measured by pumping a nanowire array that does not form a photonic crystal cavity, under the pumping condition employed for lasing and L-L curve measurements. The measured data are fitted using the fitting parameters, and $P_1 = 9.34\times10^{-3}$, $P_2 = 4.404\times10^{-6}$, and $P_3 = 0$ are extracted from the fitting. The fitting curve matches well with the measured data, as shown in Fig. S9a. IQE is then calculated using the eq.(4) as a function of pump fluence. Fig. S9b shows that the calculated IQE increases to ~40 % by increasing the pump fluence to ~20 μJ/cm^2. The quality of surface passivation is not optimized as evidenced by TRPL measurements, and improving the quality of the shell will enhance the IQE by reducing non-radiative surface recombination.

VI. Coupled mode analysis of nanowire array laser

Coupling on-chip light sources with waveguides is a crucial requirement for on-chip optical communications. As demonstrated in the manuscript, the nanowire array laser is attached to an SOI rib waveguide with the width of 440 nm and the slab height of 40 nm. Multiple cavity modes are observed from PL below the lasing threshold, which are all coupled with the waveguide and detected from the output

coupler (Fig. 4b). The electric field profiles from FDTD simulations show that the field of the fundamental mode (λ_1) is strongly confined in the center of the cavity with the coupling efficiency (η_{couple}) of 4.2 % (Fig. S10a). The Q factor of the fundamental mode (~81,000) is slightly decreased due to the additional loss through the waveguide, compared with the Q factor of the cavity simulated without the waveguide (~83,000) shown in the manuscript. The simulated electric field profiles of the second, third and fourth modes exhibit two, three and four antinodes in the cavity, and the peak wavelengths from these modes closely match with the measured data. As the in-plane confinement is weaker in the higher modes, the field couples more efficiently with the waveguides, leading to much higher coupling efficiency than the fundamental mode. This agrees well with the PL spectra measured from the output coupler. Pump position-dependent PL measurements are also conducted to further verify that the four cavity peaks observed from the PL originate from the modes described in Fig. S10a. As shown in Fig. S10b, the pump positions are shifted from the

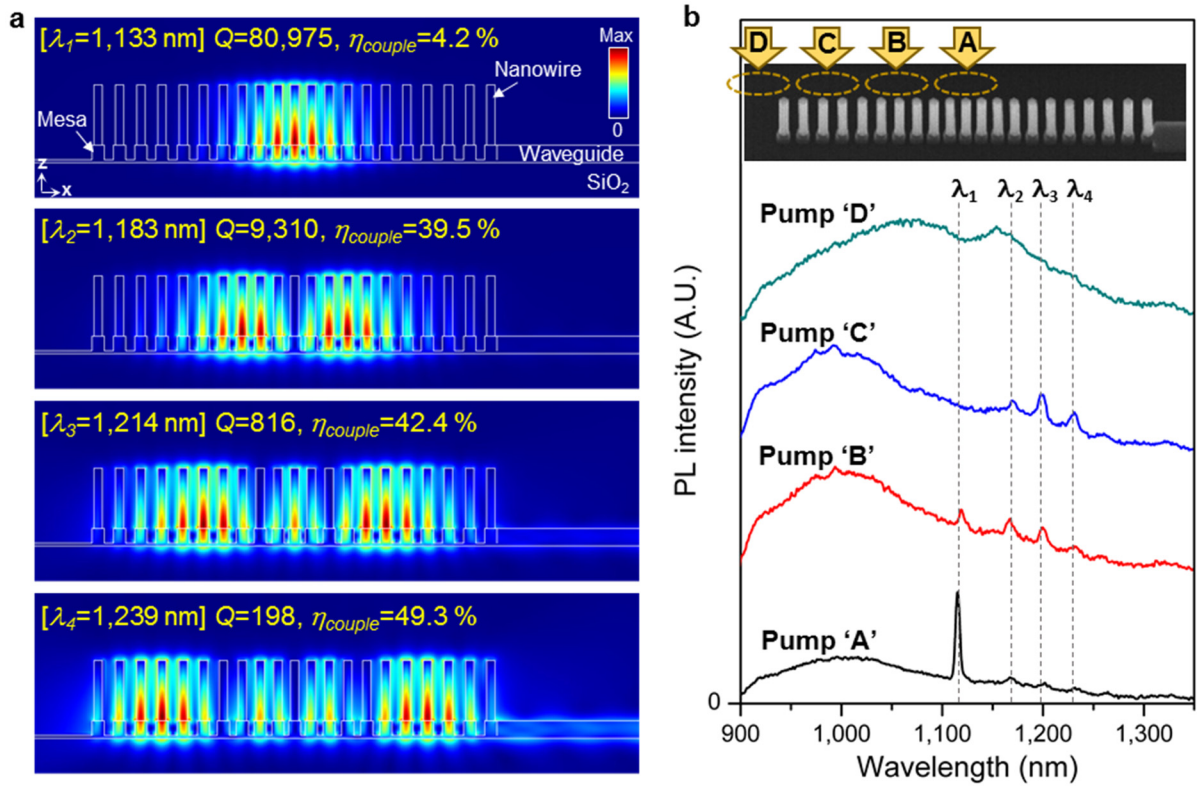


Figure S10. Multiple cavity modes of nanowire array cavity. a, Coupled mode profiles of fundamental cavity mode and higher modes. **b**, PL spectra measured at different pump positions and fixed pump fluence (88 μJ/cm^2), showing changes in relative intensities between the cavity peaks.

center (A) to the edge (D) of the cavity, maintaining the pump fluence of 88 μJ/cm^2 with an approximate pump spot size of 1.8 μm. The relative intensity of the peaks from 2nd and 3rd modes are increased when the pump position is moved from 'A' to 'B', and so do the 3rd and 4th modes when the pump position is moved from 'C' to 'D'. This is owing to the increase of the overlap between the pump area and the high-field region, which can be interpreted as the increase of the confinement factor of respective modes. Cavity peaks are not observed at the pump position 'D', because the emitted light from the nanowire at the edge is not confined but radiates freely into air. These results prove that the lasing operation occurs from the fundamental cavity mode with a single antinode in the center, while the other peaks are stemming from low-*Q* modes with multiple antinodes.

The fundamental mode exhibits a waveguide coupling efficiency of only 4.2 %, and improving the coupling efficiency will lead to higher energy efficiency for optical communications. This can be accomplished by engineering the cavity design, for example by forming asymmetric reflectors on each side of the nanobeam cavity. If the number of nanowires constituting one side of the reflector is smaller than the other side, the shorter reflector section becomes more lossy and larger portion of the field leaks through the shorter section than the other side. Thus, the coupling efficiency can be increased by removing some of the

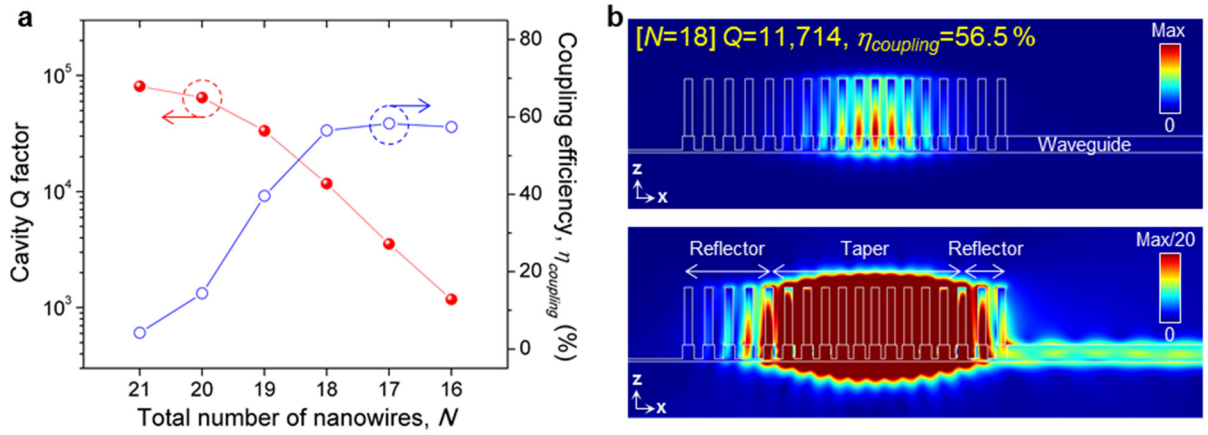


Figure S11. Asymmetric cavity for high coupling efficiency. a, Dependence of the number of nanowires constituting the cavity (*N*) on the coupling efficiency and cavity *Q*. **b**, Electric field intensity profiles of waveguide-coupled cavity mode when *N*=18 (upper), and the same field profiles rescaled to show that the energy is dominantly dissipated through the waveguide (lower).

nanowires constituting the reflector between the taper and the waveguide, whereas the cavity Q will decrease due to the larger loss. Fig. S11a shows the effect of an asymmetric cavity on the coupling efficiency and cavity Q. The Q factor is highest and the coupling efficiency is the lowest (4.2 %) in the original cavity design with 21 nanowires ($N = 21$). The coupling efficiency increases to > 50 % by sacrificing the cavity Q when the number of nanowires constituting the reflector is decreased. Nanowire-based lasers with both high coupling efficiency and reasonably high Q factor can be achieved from the asymmetric cavity design (i.e. $\eta_{couple} = 56.5\%$ and $Q \sim 12{,}000$ at $N = 18$ shown in Fig. S11b), although such asymmetric cavity is not experimentally shown because this is tangential for our proof-of-concept demonstration.

VII. References

1. Notomi, M.; Kuramochi, E.; Taniyama, H., Ultrahigh-Q nanocavity with 1D photonic gap. *Opt. Express* **2008**, 16 (15), 11095-11102.

2. Jeong, K.-Y.; No, Y.-S.; Hwang, Y.; Kim, K. S.; Seo, M.-K.; Park, H.-G.; Lee, Y.-H., Electrically driven nanobeam laser. *Nat. commun*. **2013**, 4, 2822.

3. Ahn, B.-H.; Kang, J.-H.; Kim, M.-K.; Song, J.-H.; Min, B.; Kim, K.-S.; Lee, Y.-H., One-dimensional parabolic-beam photonic crystal laser. *Opt. express* **2010**, 18 (6), 5654-5660.

4. Coldren, L. A., Corzine, S. W. & Mashanovitch, M. L., *Diode lasers and photonic integrated circuits*, John Wiley & Sons: 2012.

5. Chen, R.; Tran, T.-T. D.; Ng, K. W.; Ko, W. S.; Chuang, L. C.; Sedgwick, F. G.; Chang-Hasnain, C., Nanolasers grown on silicon. *Nat. Photonics* **2011**, 5 (3), 170-175.

6. Huang, M. H.; Mao, S.; Feick, H.; Yan, H.; Wu, Y.; Kind, H.; Weber, E.; Russo, R.; Yang, P., Room-temperature ultraviolet nanowire nanolasers. *Science* **2001**, 292 (5523), 1897-1899.

7. Xu, D.-X.; Schmid, J. H.; Reed, G. T.; Mashanovich, G. Z.; Thomson, D. J.; Nedeljkovic, M.; Chen, X.; Van Thourhout, D.; Keyvaninia, S.; Selvaraja, S. K., Silicon photonic integration platform—Have we found the sweet spot? *IEEE J. Sel. Top. Quantum Electron*. **2014**, 20 (4), 189-205.

8. Borg, M.; Schmid, H.; Moselund, K. E.; Signorello, G.; Gignac, L.; Bruley, J.; Breslin, C.; Das Kanungo, P.; Werner, P.; Riel, H., Vertical III–V nanowire device integration on Si (100). *Nano Lett.* **2014,** *14* (4), 1914-1920.

9. Li, Z.-A.; Möller, C.; Migunov, V.; Spasova, M.; Farle, M.; Lysov, A.; Gutsche, C.; Regolin, I.; Prost, W.; Tegude, F.-J., Planar-defect characteristics and cross-sections of <001>, <111>, and <112> InAs nanowires. *J. Appl. Phys.* **2011,** *109* (11), 114320.

10. Wang, J.; Plissard, S.; Hocevar, M.; Vu, T. T.; Zehender, T.; Immink, G. G.; Verheijen, M. A.; Haverkort, J.; Bakkers, E. P., Position-controlled [100] InP nanowire arrays. *Appl. Phys. Lett.* **2012,** *100* (5), 053107.

11. Cavalli, A.; Wang, J.; Esmaeil Zadeh, I.; Reimer, M. E.; Verheijen, M. A.; Soini, M.; Plissard, S. R.; Zwiller, V.; Haverkort, J. E.; Bakkers, E. P., High-Yield Growth and Characterization of ⟨100⟩ InP p–n Diode Nanowires. *Nano Lett.* **2016,** *16* (5), 3071-3077.

12. Kim, H.; Farrell, A. C.; Senanayake, P.; Lee, W.-J.; Huffaker, D. L., Monolithically integrated InGaAs nanowires on 3D structured silicon-on-insulator as a new platform for full optical links. *Nano Lett*. **2016**, 16 (3), 1833-1839.

13. Shapiro, J.; Lin, A.; Wong, P.; Scofield, A.; Tu, C.; Senanayake, P.; Mariani, G.; Liang, B.; Huffaker, D., InGaAs heterostructure formation in catalyst-free GaAs nanopillars by selective-area metal-organic vapor phase epitaxy. *Appl. Phys. Lett*. **2010**, 97 (24), 243102.

14. Komolibus, K.; Scofield, A. C.; Gradkowski, K.; Ochalski, T. J.; Kim, H.; Huffaker, D. L.; Huyet, G., Improved room-temperature luminescence of core-shell InGaAs/GaAs nanopillars via lattice-matched passivation. *Appl. Phys. Lett.* **2016,** *108* (6), 061104.

15. Yoo, Y.-S.; Roh, T.-M.; Na, J.-H.; Son, S. J.; Cho, Y.-H., Simple analysis method for determining internal quantum efficiency and relative recombination ratios in light emitting diodes. *Appl. Phys. Lett.* **2013,** *102* (21), 211107.

16. Saxena, D.; Mokkapati, S.; Parkinson, P.; Jiang, N.; Gao, Q.; Tan, H. H.; Jagadish, C., Optically pumped room-temperature GaAs nanowire lasers. *Nat. Photonics* **2013,** *7* (12), 963-968.